Supporting Info for

Imparting Gas selective and pressure dependent porosity into a non-porous solid via coordination flexibility

Shyamapada Nandi,[a,c] Phil De Luna,[c] Rahul Maity,[a] Debanjan Chakraborty,[a] Thomas Daff,[c] Thomas Burns,[c] Tom K. Woo,[c*] Ramanathan Vaidhyanathan,[a,b *]

[a] Department of Chemistry, Indian Institute of Science Education and Research, Pune, India.
[b] Centre for energy, Indian Institute of Science Education and Research, Pune, India.
[c] Centre for Catalysis Research and Innovation, Department of Chemistry, University of Ottawa, Canada.

*Correspondence to: vaidhya@iiserpune.ac.in, twoo@uottawa.ca

Table of contents:

1. Materials and methods

All the organic chemicals were purchased from sigma aldrich. The metal salts were procured from Alfa Aesar. Compounds and solvents were all used without any further purification.

<u>Milligram scale synthesis:</u>

*Synthesis of Mg 4-PyC(**1**):*

A solvothermal reaction between magnesium acetate tetra hydrate (0.215 g; 1 mmol) and pyridine-4-carboxylic acid (0.244 g; 2 mmol) in a solution containing 5 ml dimethylformamide (DMF) +3mlacetonitrile was carried out at 120^{o} C for 72 hrs. Colorless cube shape crystals were isolated by filtration and were washed with plenty of acetone. The air dried sample gave a yield of ~85% (0.258g; 0.42mmol) based on Mg. The PXRD pattern indicated this to be a pure phase of **1**. We have also prepared 10-25 g of this sample with an easy scale-up procedure. CHN analysis (calculated values within brackets): C: 53.41 (53.15); H: 4.03 (3.80); N: 11.20 (11.48) %.Though it was made in DMF medium it could be exchanged in a post synthetic manner with DCM or it can be directly activated at 160^{o} C under vacuum. Also, the use of dimethylacetamide (DMA) instead of DMF led to the same phase of **1.**

*Synthesis of Mn 4-PyC(**2**):*

A solvothermal reaction between manganese acetate tetra hydrate (0.245g; 1mmol) and pyridine-4-carboxylic acid (0.244 g; 2 mmol) in a solution containing 5 ml DMF + 3 ml acetonitrile was carried out at 120^{o}C for 72hrs. Colorless rod shape crystals were isolated by filtration and were washed with plenty of acetone. The air dried sample gave a yield of ~85% (0.283g; 0.42mmol) based on Mn. The PXRD pattern indicated this to be a pure phase of **2**. We have also prepared 10-25gms of this sample with an easy scale-up procedure. CHN analysis (calculated values within brackets): C: 48.58 (48.30); H: 3.66 (3.45); N: 10.26 (10.43) %.Though it was made in DMF medium it could be exchanged in a post synthetic manner with DCM or it can be directly activated at 160^{o}C under vacuum. Also, the use of DMA instead of DMF led to the same phase of **2**.

*Synthesis of Cu 4-PyC(**3**):*

A solvothermal reaction between copper acetate mono hydrate (0.200g; 1mmol) and pyridine-4-carboxylic acid (0.244 g; 2 mmol) in a solution containing 2 ml DMF + 2 ml ethanol+ 3 ml tetrahydrofuran was carried out at 110^{o} C for 72 hrs. Blue color cube shape crystals were isolated by filtration and were washed with plenty of acetone. The air dried sample gave a yield of ~80% (0.304g; 0.80mmol) based on Cu. The PXRD pattern indicated this to be a pure phase of **3**. CHN analysis (calculated values within brackets) : C: 49.22 (48.91); H: 3.21 (3.52); N: 7.90 (8.15) %.Though it was made in DMF medium it could be exchanged in a post synthetic manner with DCM or it can be directly activated at 140° C under vacuum. Also, the use of DMA instead of DMF led to the same phase of **3.**

10gm scale synthesis:

*Synthesis of Mg 4-PyC(**1**):*

About 5.33 g of magnesium acetate tetra hydrate was added to 6.08 g of 4-PyC in a solution containing 40 ml DMF + 30 ml acetonitrile; contents were stirred for 2.5 hrs at room temperature. Contents were placed in a 123 ml Teflon-lined Parr stainless steel autoclave and heated at 130° C for 72 hrs. Colorless polycrystalline product identical in appearance to the small scale preparation was obtained.

*Synthesis of Mn 4-PyC(**2**):*

About 6.10g of magnesium acetate tetra hydrate was added to 6.08 g of 4-PyC in a solution containing 40 ml DMF + 30 ml acetonitrile; contents were stirred for 2.5 hrs at room temperature. Contents were placed in a 123 ml Teflon-lined Parr stainless steel autoclave and heated at 130° C for 72 hrs. Colorless polycrystalline product identical in appearance to the small scale preparation was obtained.

2. Single crystal structure determination:

Single-crystal data was collected on a Bruker SMART APEX four-circle diffractometer equipped with a CMOS photon 100 detector (Bruker Systems Inc.) and with a Cu Kα radiation (1.5418 Å). The incident X-ray beam was focused and monochromated using Microfocus (IμS). Crystals were mounted on nylon Cryo loops with Paratone-N oil. Data was collected at 100(2) K. Data was integrated using Bruker SAINT software and was corrected for absorption using SADABS. Structure was solved by Intrinsic Phasing module of the direct methods and refined using the SHELXTL 97 software suite. All non-hydrogen atoms were located from iterative examination of difference F-maps following which the structure was refined using least-squares method. Hydrogen atoms were placed geometrically and placed in a riding model. In case of VT XRD with a single crystal, only the cell parameters were determined as a function of temperature.

Table S1. Unit cell parameters for Mg 4-PyC, Mn 4-PyC and Cu 4-PyC.

Materials	a (Å)	b (Å)	c (Å)	α (◦)	β(◦)	γ(◦)	V (Å^3)	Sp.Gr
Mg 4-PyC	9.8763(6)	13.0177(9)	10.6775(7)	90.00	100.843(2)	90.00	1348.26(15)	P2(1)
Mn 4-PyC	9.9665(4)	13.2955(5)	10.6833(4)	90.00	103.110(2)	90.00	1378.74(9)	P2(1)
Cu 4-PyC	11.4487(8)	12.3600(8)	12.3919(8)	90.00	117.201(3)	90.00	1559.60(18)	P2(1)/c

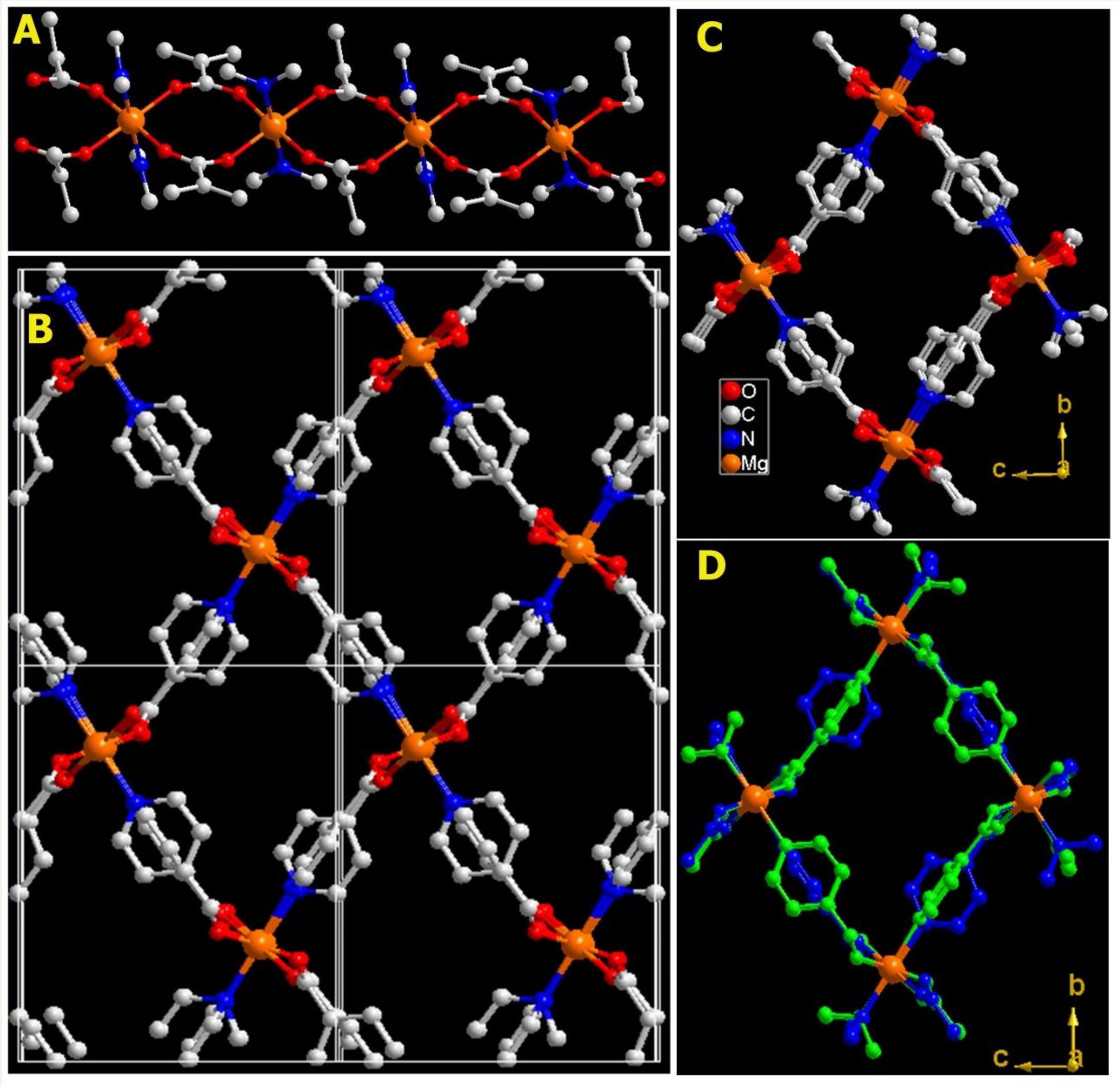

Figure S1. (A) Basic building unit of **1**. Each Mg is octahedrally coordinated. (B) The three-dimensional structure of **1**viewed along the a-axis. (C) Three-dimensional structure showing a single channel. (D) The channel where two different orientation of the linker has been represented in different colors.

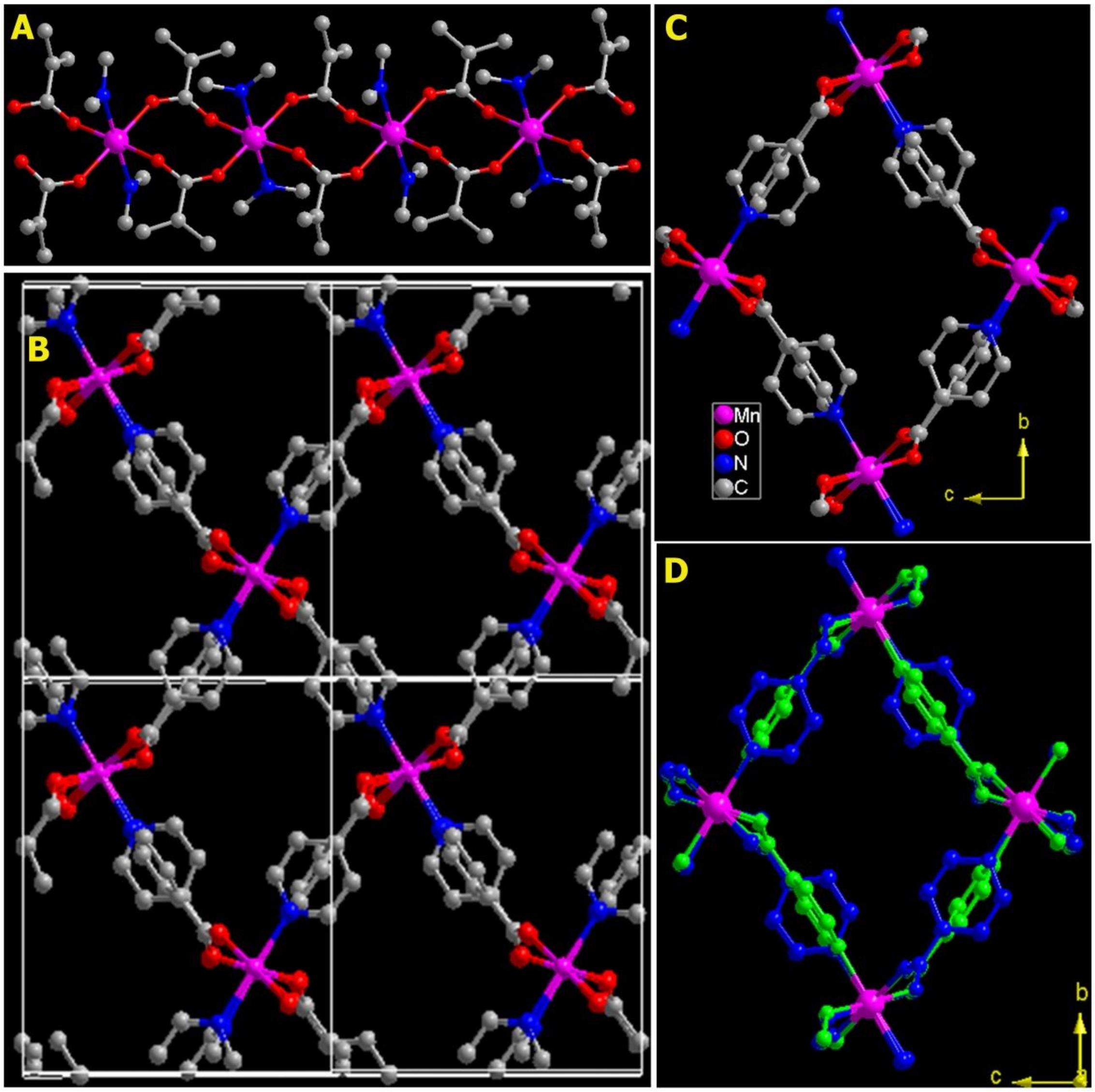

Figure S2. (A) Basic building unit of **2**. Each Mn is octahedrally coordinated. (B) The three-dimensional framework of **2** viewed along the a-axis. (C) Structure of **2** showing a single channel formed by the linking of isolated metal octahedral by the 4-PyC units. (D) The 1-D channel along the a-axis, where two different orientation of the linker has been presented with different colors.

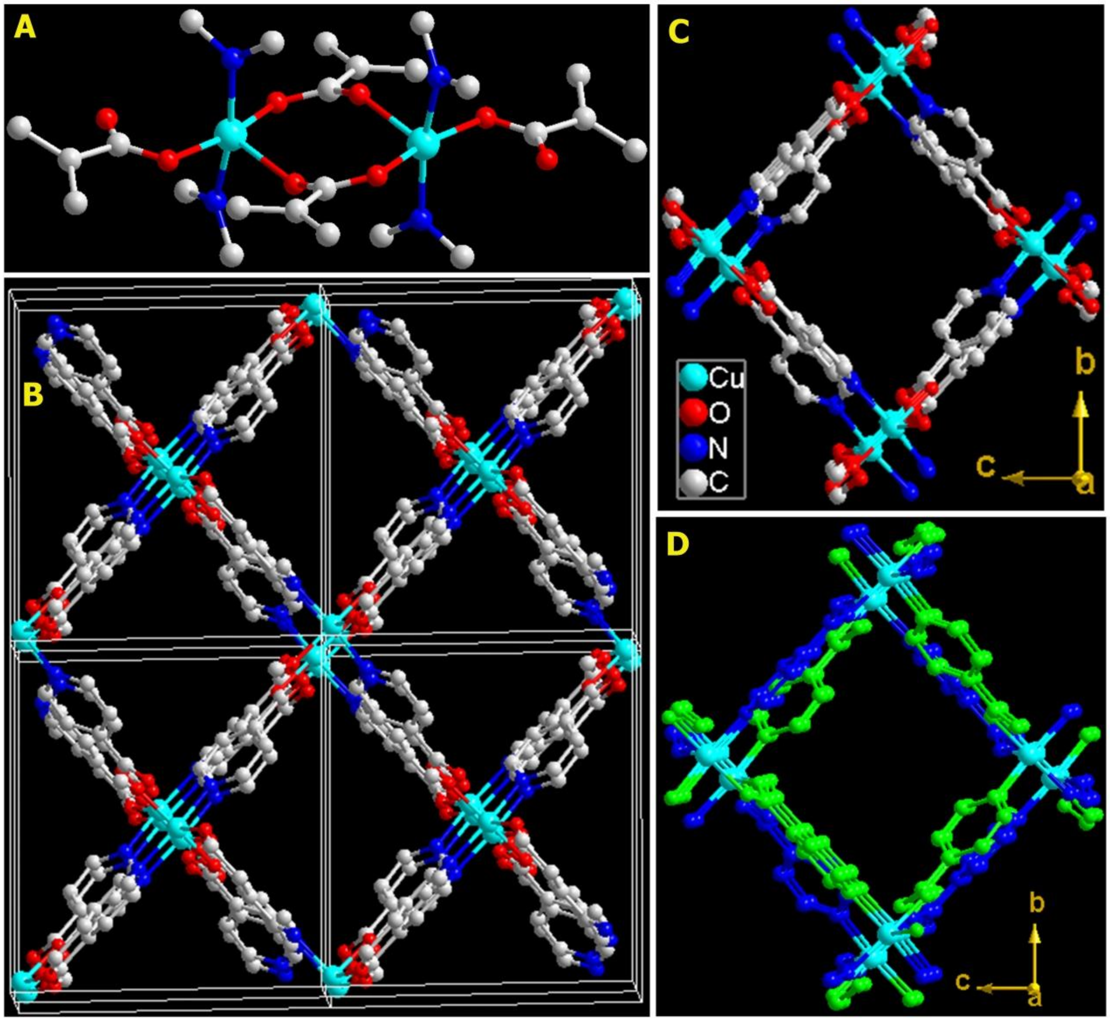

Figure S3. (A) Basic building unit present in **3**. Unlike other two cases, here the Cu adopts a pentagonal pyramidal coordination geometry. (B) The three-dimensional structure of **3** along the a-axis. (C) The 1-D channels running along the a-axis in**3**. (D) The two different orientation of the linker 4-PyC haves been presented with different colors. Here, two linkers are not oriented in 90° to each other; rather the orientation is almost the same for these crystallographically independent linker units.

From the Figure S3A, the building unit can be seen to have Cu-carboxylate chain formed by equatorially positioned carboxylates and two pyridyl groups occupying the axial positions of the Cu^{2+} centers. Now, at each Cu^{2+} site, the pyridyl-linkers in the axial position, might have a better overlap with the Cu^{2+}'s e_g^3 orbitals, and thereby provide the Jahn-Teller stabilization, leading to a relatively stronger bond. Hence the rotation about this bond is arrested resulting in a rigid open-form. Thus, the increased stability for the Cu-N bonds compared to the Mg-N and Mn-N bonds could be coming from a combination of HSAB and J-T effects.

3. Analytical characterizations

Powder X-ray diffraction:

Powder XRDs were carried out using a Rigaku Miniflex-600 instrument and processed using PDXL software. All the high temperature PXRD was recorded using powder sample on a platinum plate. However, all the other PXRD were recorded using powder sample on a zero background glass holder. For the PXRD under CO_2 environment, the sample was put inside a small air tight environmental cell with a Kapton foil. The XRD was recorded after dosing the cell with 1 bar of CO_2.

Thermo gravimetric Analysis:

Thermogravimetry was carried out on NETSZCH TGA-DSC system. The routine TGAs were done under N_2 gas flow (20 ml/min) (purge + protective) and samples were heated from RT to 550° C at 2 K/min.

For the cycling experiments, no protective gas was used, and the gas flows were systematically switched between CO_2 and N_2 on the purge lines. The methanol exchanged and activated (160° C, 15 hrs) sample of **1** was loaded on to the Pt pans and evacuated for 5 hrs prior to the runs. TGA and DSC calibration and base-line corrections runs were done before carrying out the cycling experiments.

Infrared (IR) spectroscopy:

IR spectra were obtained using a Nicolet ID5 attenuated total reflectance IR spectrometer operating at ambient temperature. The KBr pellets were used as background blanks.

Powder X-ray diffraction:

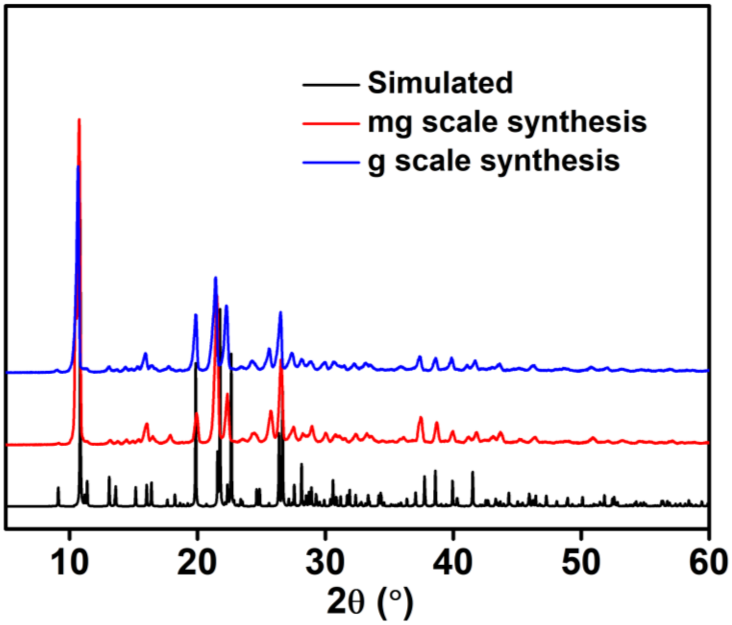

Figure S4. Comparison of the experimental powder X-ray diffraction (PXRD) patterns of **1**(small scale and large scale) with the patterns simulated from the single crystal x-ray diffraction.

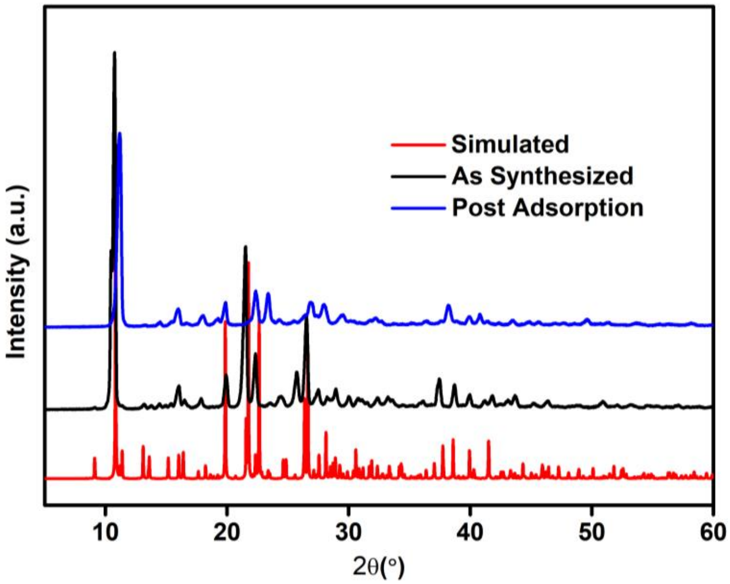

Figure S5. Comparative PXRD of **1:** Simulated vs. as-synthesized as well as the post-adsorption sample. Note that **1** is exceptionally stable to heating under vacuum (activation during adsorption-desorption cycles).

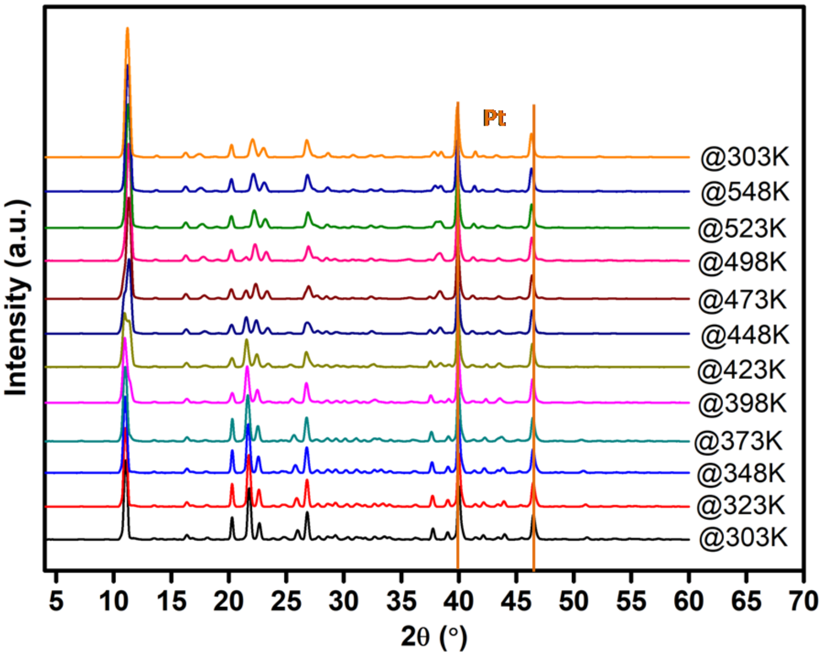

Figure S6. Variable temperature PXRD of **1**. The material possesses exceptional thermal stability**.** The peak around 2θ = 40° and 47° is due to reflection from the platinum plate (from the sample holder).

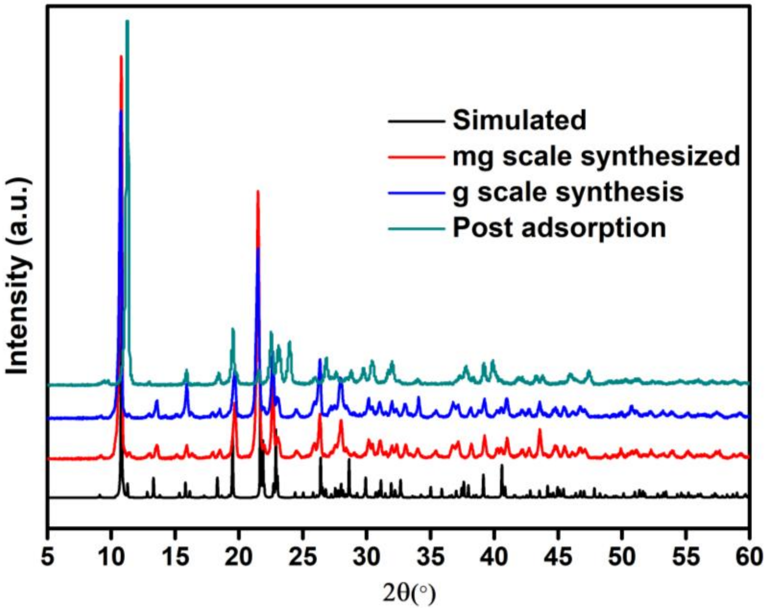

Figure S7. Comparison of the PXRD of **2:** Simulated vs. as-synthesized as well as the post-adsorption sample. Note that **2** is exceptionally stable to heating under vacuum.

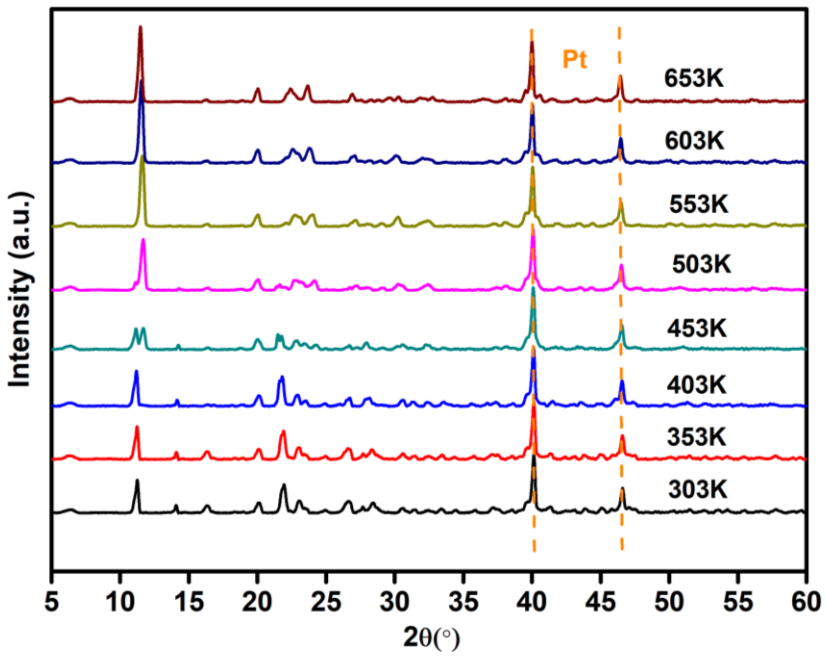

Figure S8. Variable temperature PXRD of **2**. The material shows exceptional thermal stability just like **1.** Platinum peaks are from the sample holder.

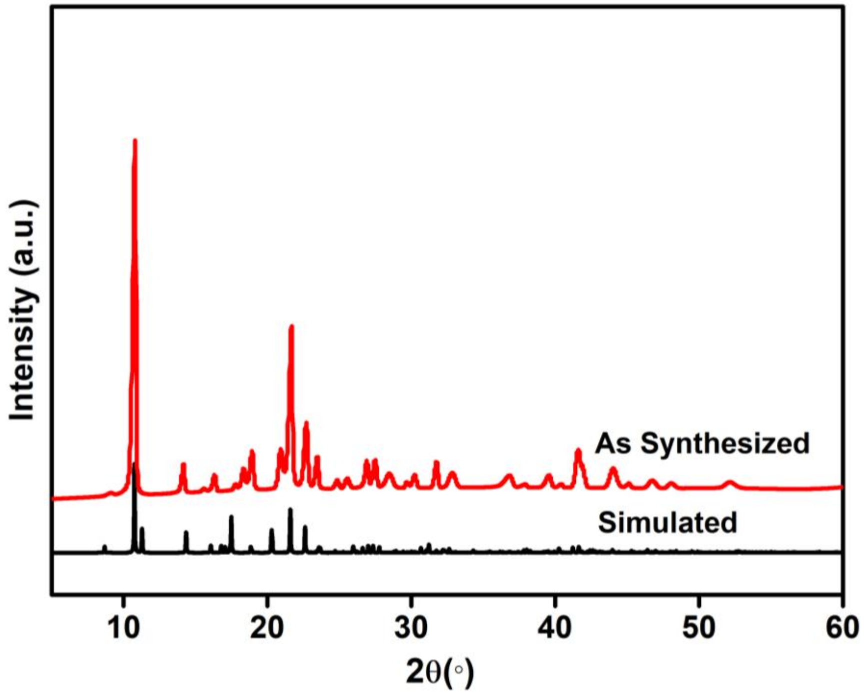

Figure S9. Comparative PXRD of **3:** Simulated vs. as-synthesized sample.

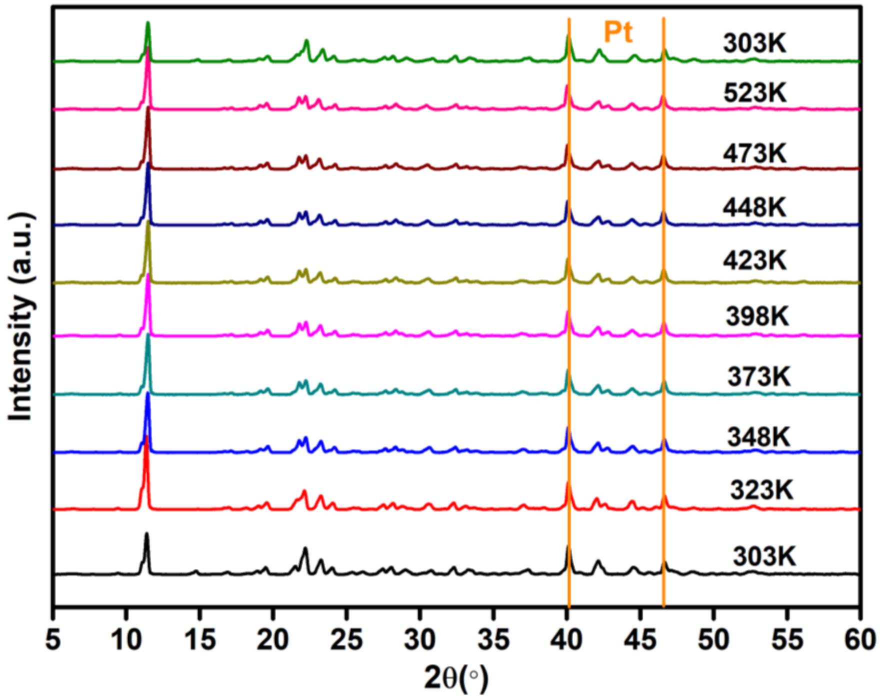

Figure S10. Variable temperature PXRD of **3.** Peaks due to the Pt plate (sample holder) are observed.

Thermo gravimetric analysis (TGA):

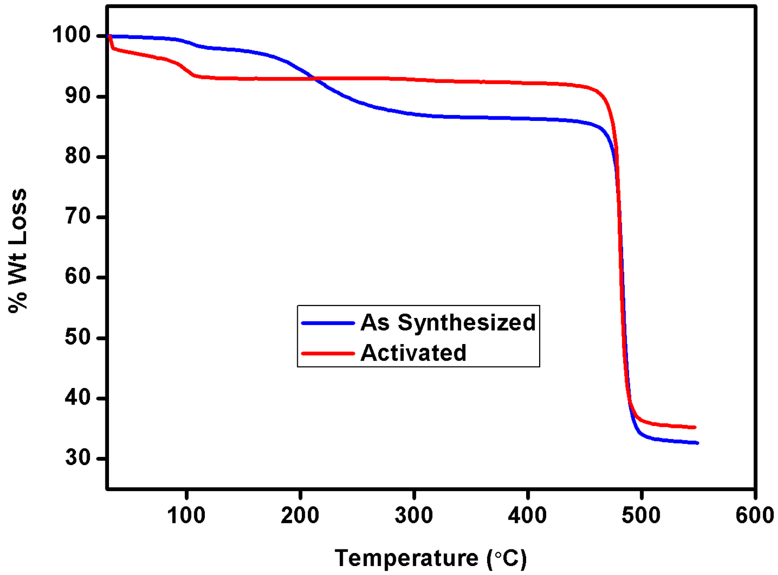

Figure S11. TGA plots of the as-made **1** and the completely activated (solvent exchanged and heated at 150° C for 24 hrs under vacuum) sample.

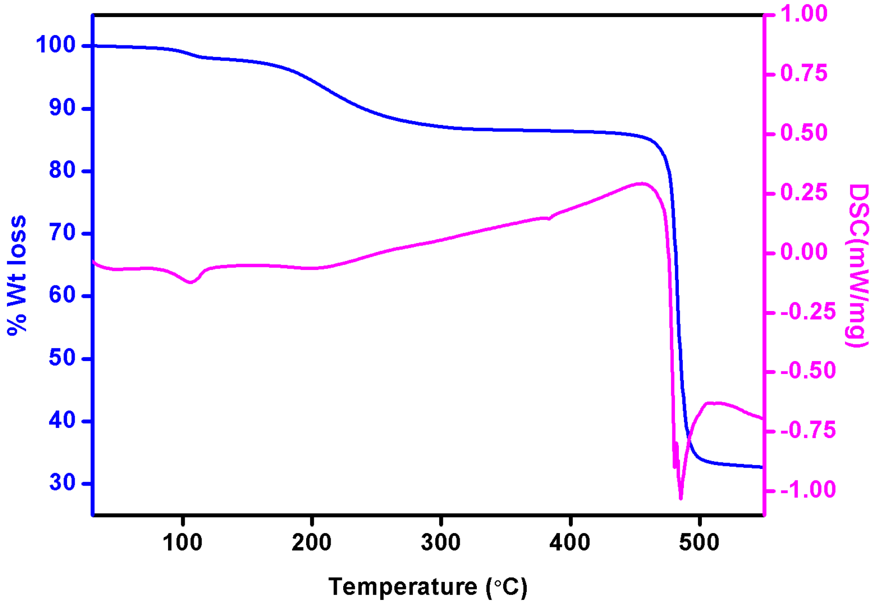

Figure S12. TGA carried out on the as-synthesized sample of **1**. The weight loss has been calculated using the formula $Mg_2(C_6NH_4O_2)_4(C_3H_7NO)$ (M. Wt. **610.11 g/mol**). All the surface solvent molecules are removed by 100° C (loss ~2 %), while most of the free DMF molecules come off at 180° to 230° C (calc: 9.61 %; obsd: 11.19 %). Note that the framework exhibits exceptional thermal stability up to 480° C.

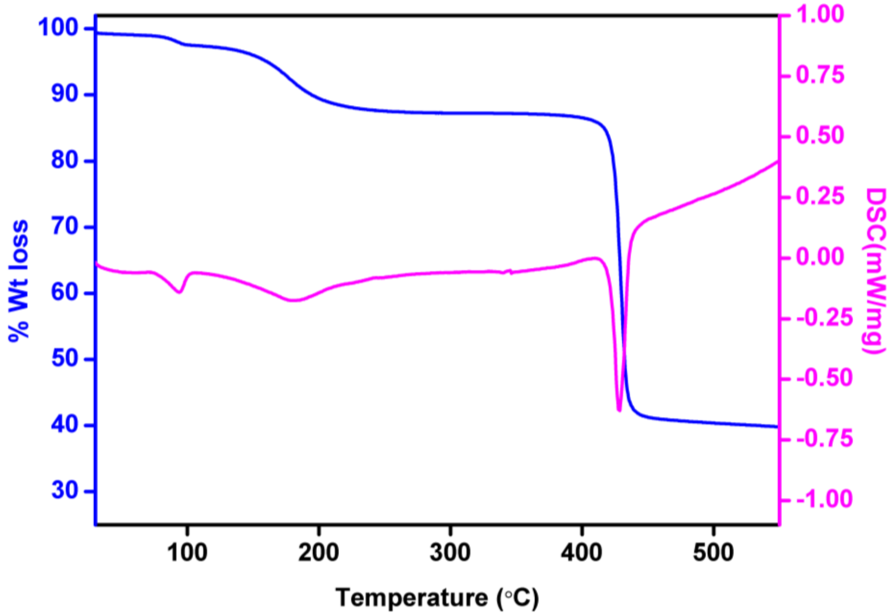

Figure S13. TGA carried out using the as-synthesized sample of **2**. The weight loss has been calculated using the formula $Mn_2(C_6NH_4O_2)_4(C_3H_7NO)$ (M. Wt. **671.37 g/mol**). All the surface solvent molecules are removed by 100° C (loss ~2 %), while most of the free DMF come off at 180° to 230° C (calc: 10.87 %; obsd: 10.49 %). Note that the framework exhibits exceptional thermal stability up to 420° C.

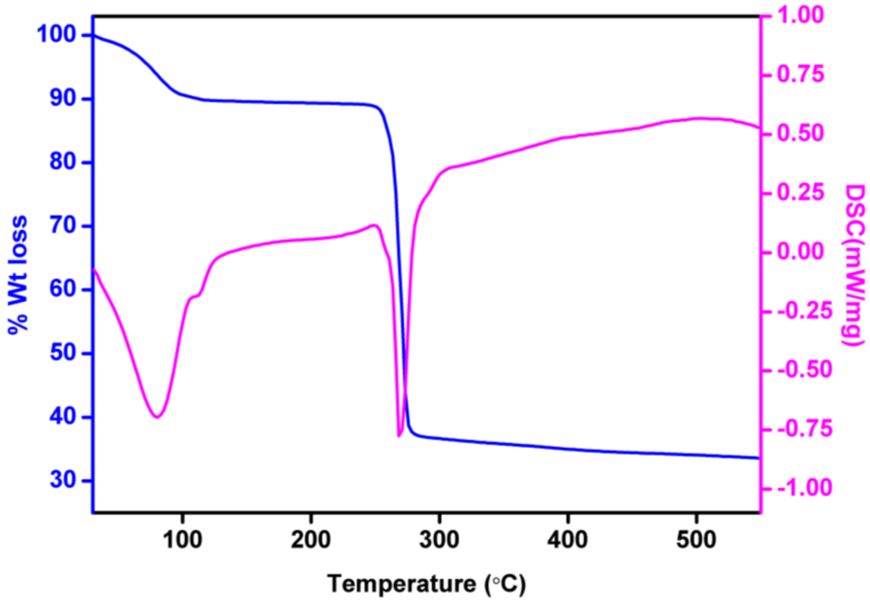

Figure S14. TGA carried out on the as synthesized sample of **3**. The weight loss has been calculated using the formula $Cu_2(C_6NH_4O_2)_4(C_4H_8O)$ (M. Wt. **687.60 g/mol**). All the solvent molecules, THF, are removed by 100° C (calc: 10.61 %; obsd: 10.91 %). Note that the framework exhibits exceptional thermal stability up to 260° C.

TGA cycling experiment:

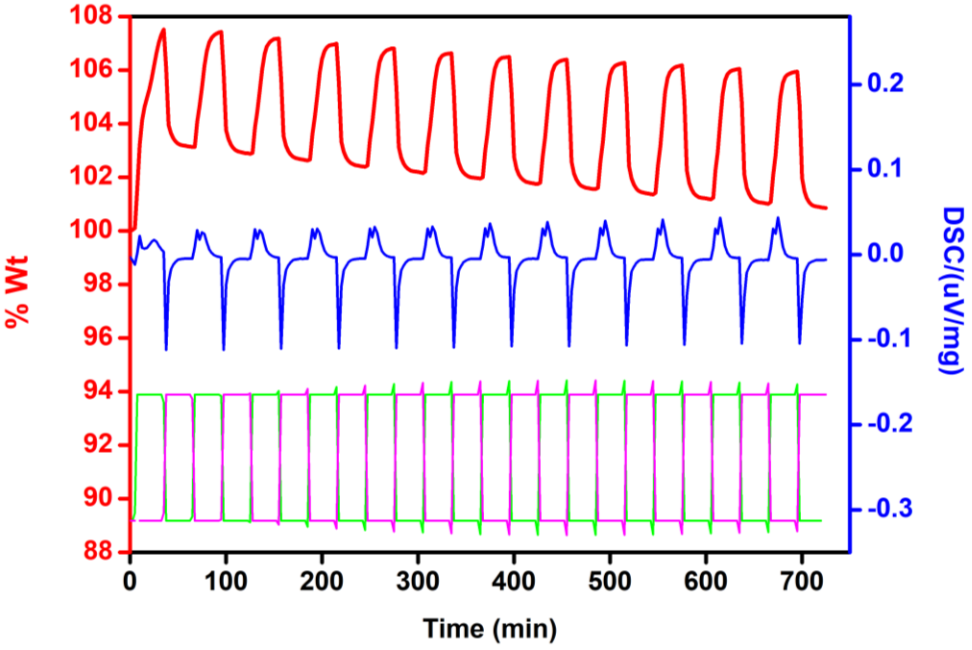

Figure S15. CO_2/N_2 cycling experiment using **1.** Flow rate used was 20 ml/min. DSC traces show two different peak- could be due to the presence of two different but closely related adsorption sites.

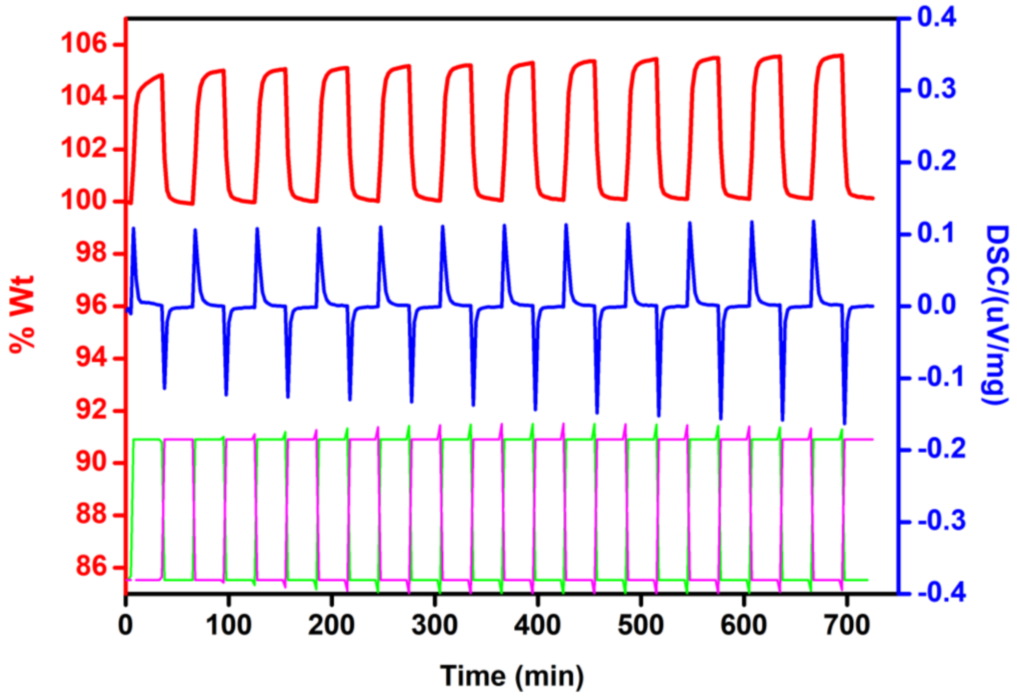

Figure S16. CO_2/N_2 cycling experiment using **1.** Flow rate used was 50 ml/min. DSC traces showing two different peak.

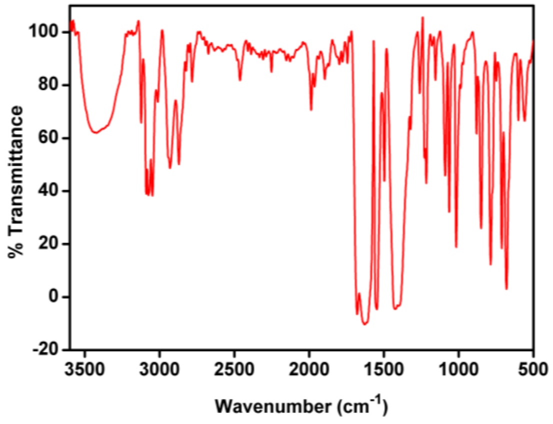

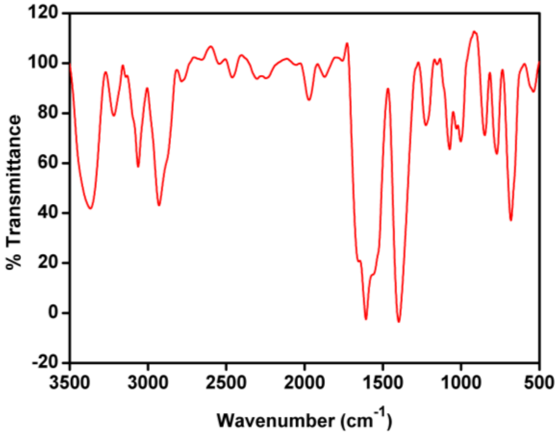

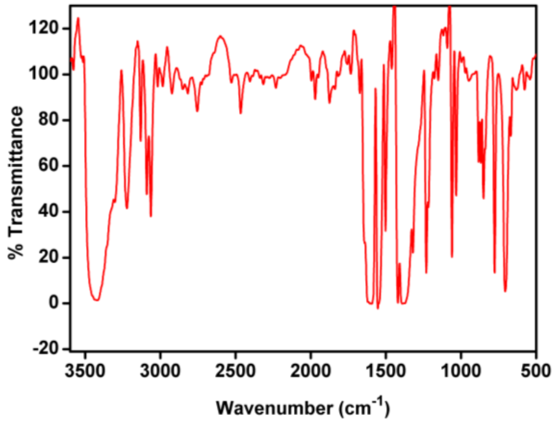

Figure S17. Infra-red spectra of **1**, **2** and **3** showing the various stretching and bending modes present. Selected peaks: IR (KBr pellet, cm^{-1}): v(O-H) solvent: 3465; v(C-H): 2992; v(COO): 1658 and 1598, v(C=C): 1208 to 800. (Source: Infrared and Raman Spectra of Inorganic and Coordination Compounds, Part B, Applications in Coordination, Organometallic, and Bioinorganic Chemistry, 6th Edition, Kazuo Nakamoto)

4. Adsorption Analysis

All gas sorption isotherms were measured on a Micromeritics ASAP 2020HD or 3-FLEX instrument using ultra-high purity gases (≥4.8 grade). Samples were transferred to a glass tube for analysis, with dual stage activation: The as-made samples were solvent exchanged by soaking 200 mg in 7 ml DCM (reagent grade) for 24 hours, with the solvent being replenished every 6hrs. Following this ~100 mg of the solvent exchanged sample was transferred to an analysis glass vial and evacuated at 180^{o}C on the degas port for 36hrs (10^{-6} mbar), at which point the outgas rate was ≤ 2 µbar/min.

The rate of adsorption experiments were carried out on the Micromeritics ASAP2020HD instrument equipped with a ROA software capabilities. Numerous equilibrium points and associated kinetic data were recorded at 273 K. For data analysis, regularly spaced 10CO_2 loading points were picked in the interval of 0 to 1000 mbar.

Table S2. Adsorption and desorption data for 195 K CO_2

Absolute Pressure (mmHg)	Amount adsorbed (mmol/g)
0.331270248	0.543809612
1.012192369	1.877483828
2.017788887	2.867530286
2.779516935	3.098605084
4.641766071	3.385548277
7.9339118	3.575026545
13.01223087	3.758892186
17.40641594	3.808977669
21.56363106	3.837914367
28.99429703	3.860039063
36.01469803	3.882058933
48.20235062	3.906672115
60.03760529	3.933636105
70.17875671	3.95223758
80.08010101	3.966506205
90.18074036	3.981945257
100.3346863	3.997525435
114.5876541	4.012275073
128.9645538	4.028766234

136.2297668	4.039437249
143.3015289	4.049635405
157.621582	4.06718715
171.9382324	4.082963445
186.3448486	4.097537832
200.4986572	4.110125408
214.7712555	4.126552196
229.2537079	4.143534093
243.7911987	4.158862037
272.461853	4.181423175
301.3612366	4.209319306
329.68573	4.237730309
343.9915771	4.255377354
358.1341858	4.273777981
386.572937	4.298031714
415.5287781	4.325638888
443.9020691	4.352484439
472.4134827	4.380422859
501.1263428	4.411545041
530.0723877	4.445076977
559.321106	4.481042125
587.9716797	4.515962745
616.5640869	4.551426555
645.7827759	4.590157791
674.7662354	4.624035342
702.2460327	4.658147638
665.7689819	4.6280629
635.1241455	4.603871199
604.1782837	4.5783839
574.8915405	4.5567397
543.8469238	4.531805898
513.2229004	4.512110885
482.3674011	4.494519177
451.4325562	4.477380319
420.5057983	4.457237546
389.8466797	4.436293827
358.8648071	4.417482358
328.1066284	4.400371055
296.2582703	4.385290686
265.0784302	4.369985975
234.3279419	4.354046393
204.8252869	4.340208742
173.9718475	4.327308083
143.085556	4.313831494

112.2762375	4.301115955
81.51797485	4.289087003
50.77935028	4.26836934
35.01835251	4.251142493
19.70196533	4.23186596
12.04301167	4.210029297
4.473938942	4.161871179

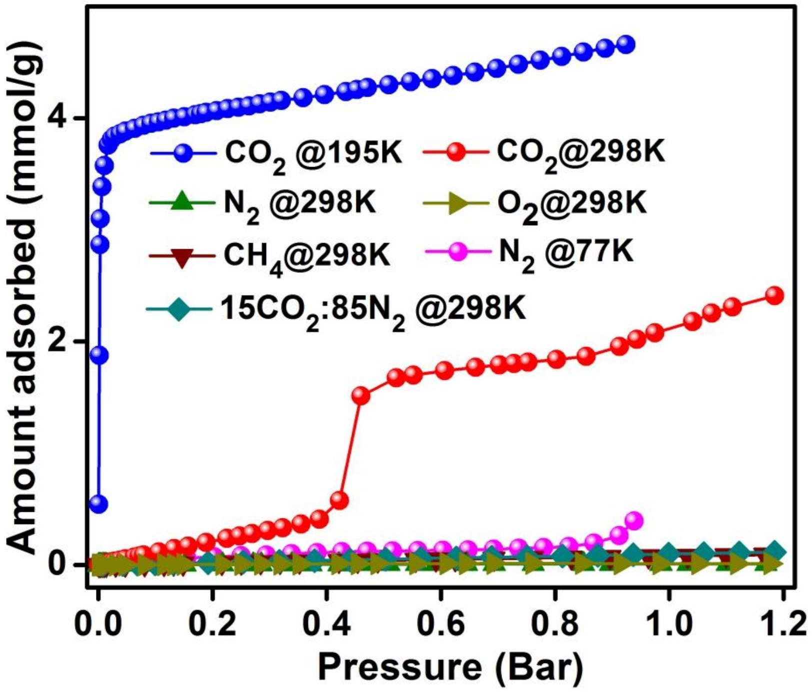

Figure S18. CO_2, N_2,CH_4, O_2 and Flue gas adsorption isotherms of **1.** Note that only CO_2 is able to acces the nanospace through gate opening.

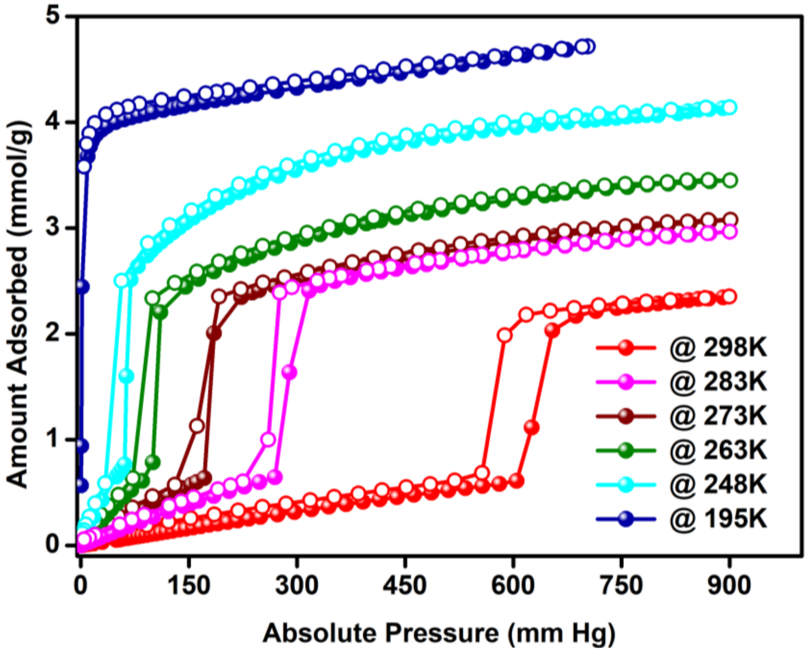

Figure S19. CO_2 adsorption/desorption isotherms of **2** at different temperatures showing the gating at different pressures of CO_2.

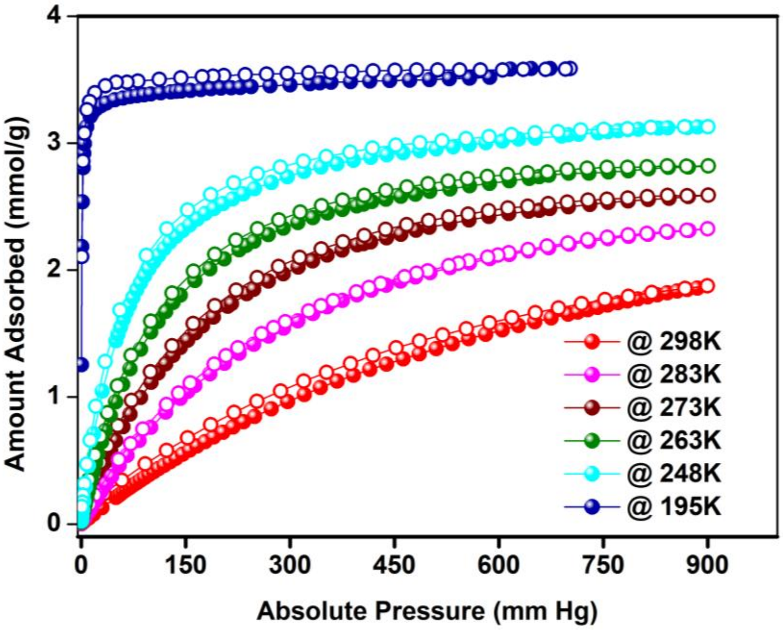

Figure S20. CO_2 adsorption/desorption isotherms of **3** at different temperatures showing no gating. This is due to the fact that in this case material is already in *open pore* configuration. The stronger N-Cu bond needs more energy compared to other two cases and thats why CO_2 is not showing any gating phenomenon.

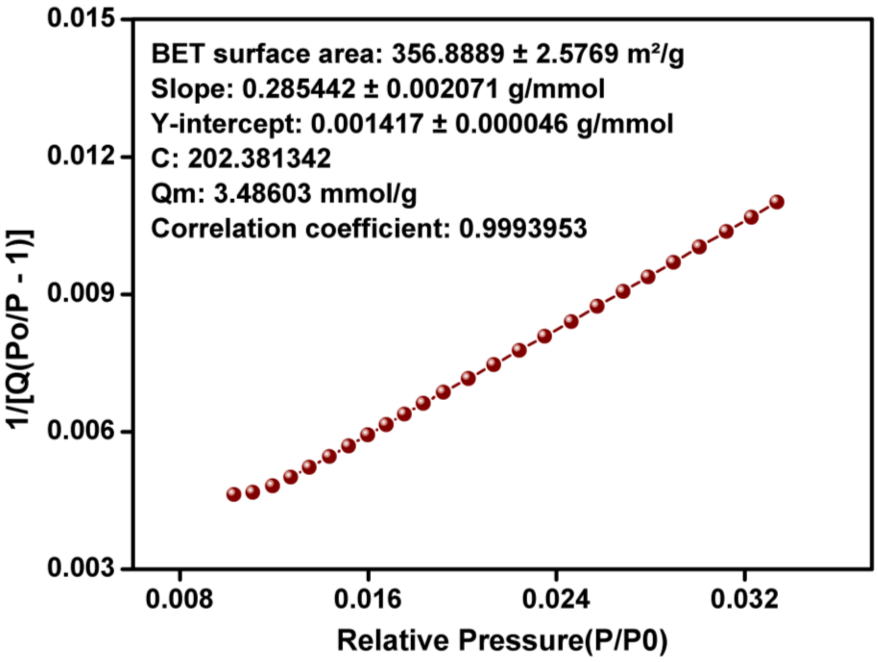

Figure S21. BET surface area fit for **1** calculated using the 273 K CO_2 adsorption isotherm.

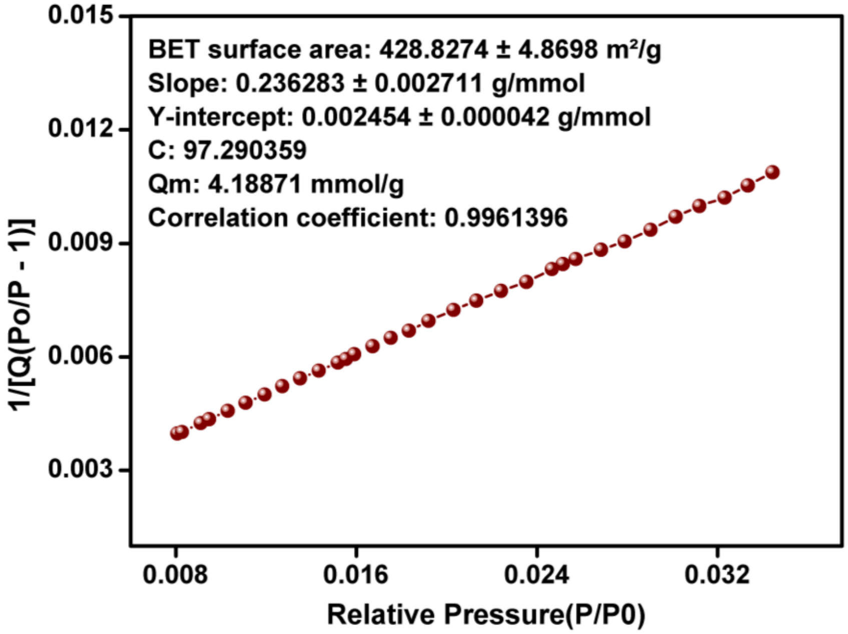

Figure S22. BET surface area fit for **2** calculated using the 273 K CO_2 adsorption isotherm.

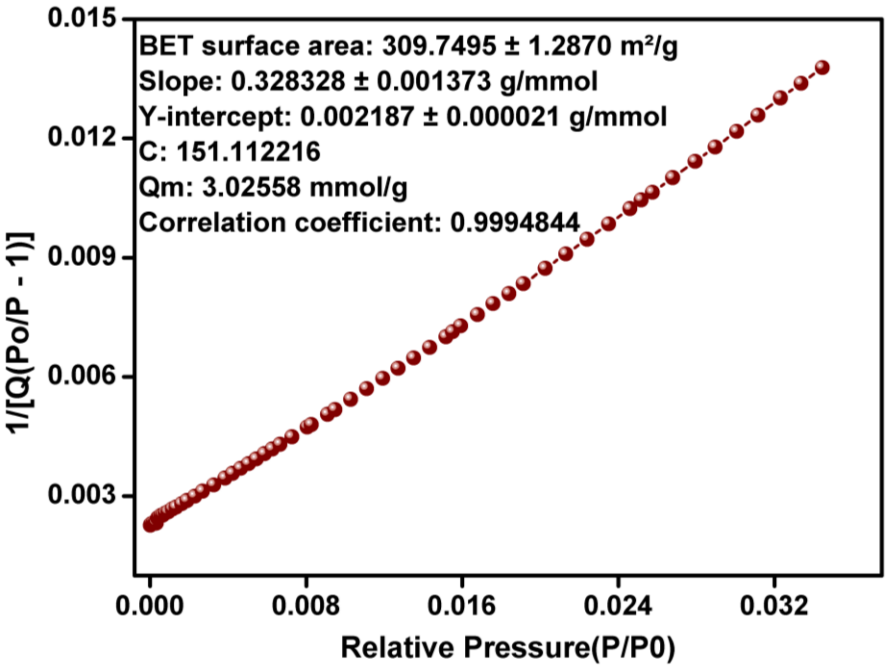

Figure S23. BET surface area fit for **3** calculated using the 273 K CO_2 adsorption isotherm.

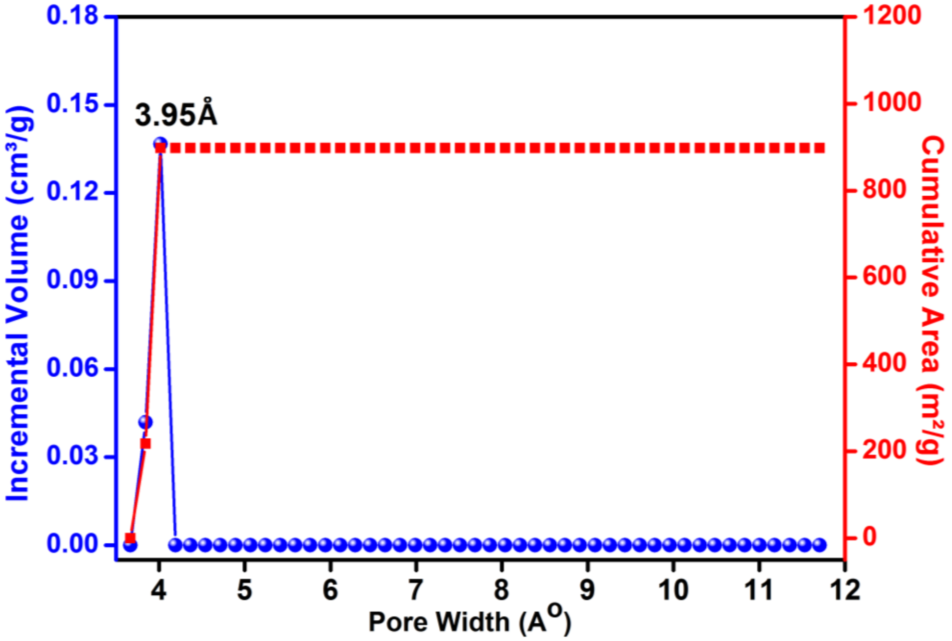

Figure S24. Pore size distribution (NLDFT, Slit pore model) of **1** calculated using the 195 K CO_2 adsorption isotherm.

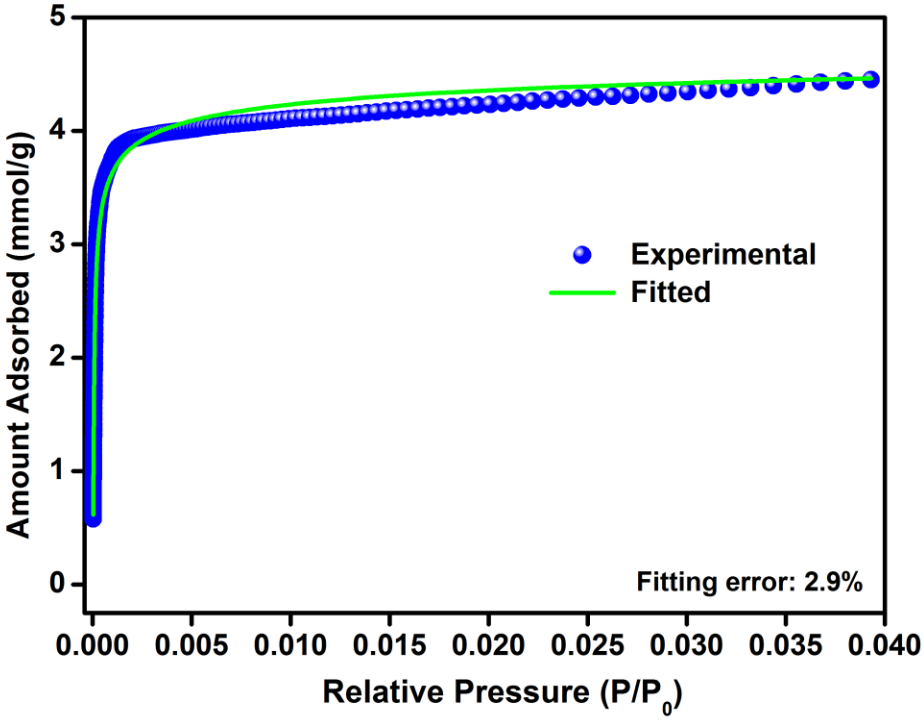

Figure S25. NLDFT fitting comparision for **1**. Note that an average fit was obtained using the entire range of data points of the 195 K CO_2adsorption isotherm.

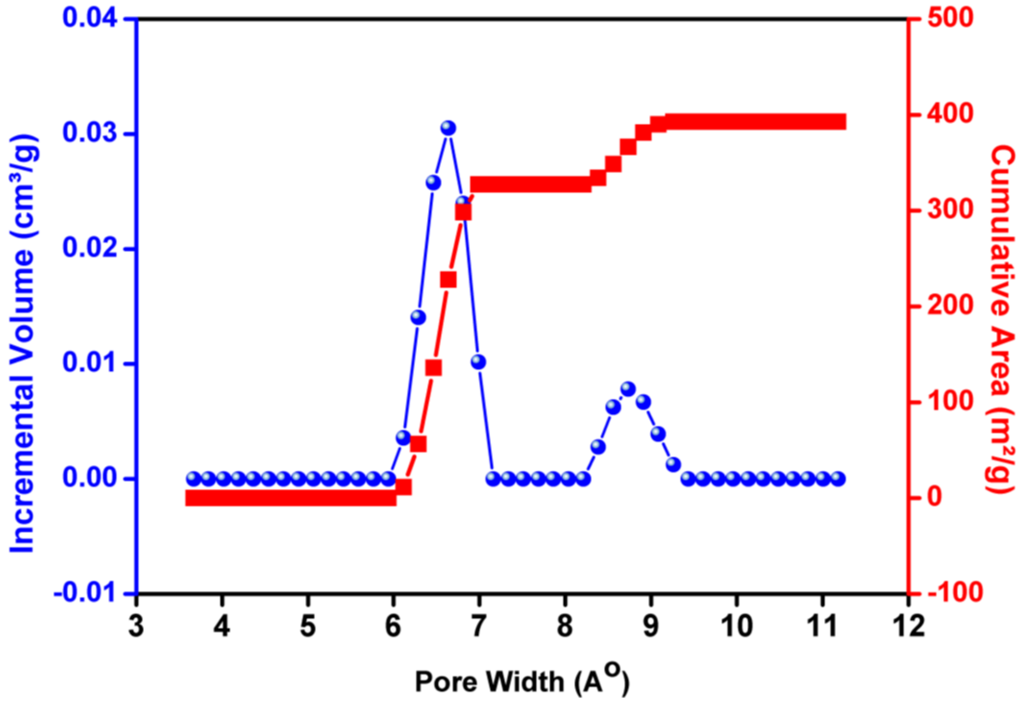

Figure S26. Pore size distribution (NLDFT Slit pore model) of **1** calculated using the 273 K CO_2 adsorption isotherm.

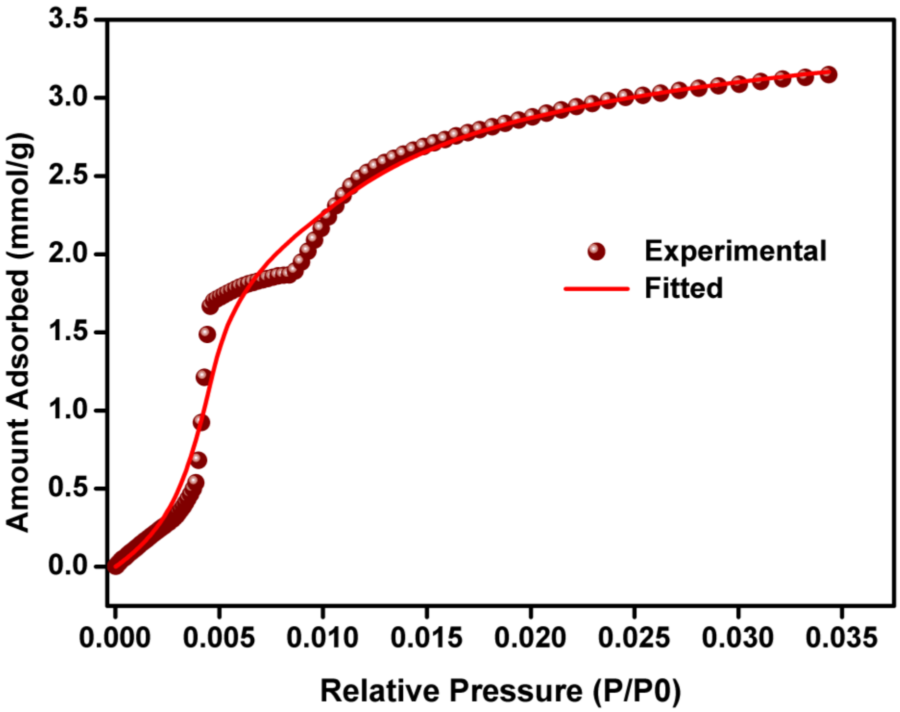

Figure S27. NLDFT fitting comparision for **1**. Note that an average fit was obtained using the entire range of data pointsof the 273 K CO_2 adsorption isotherm.

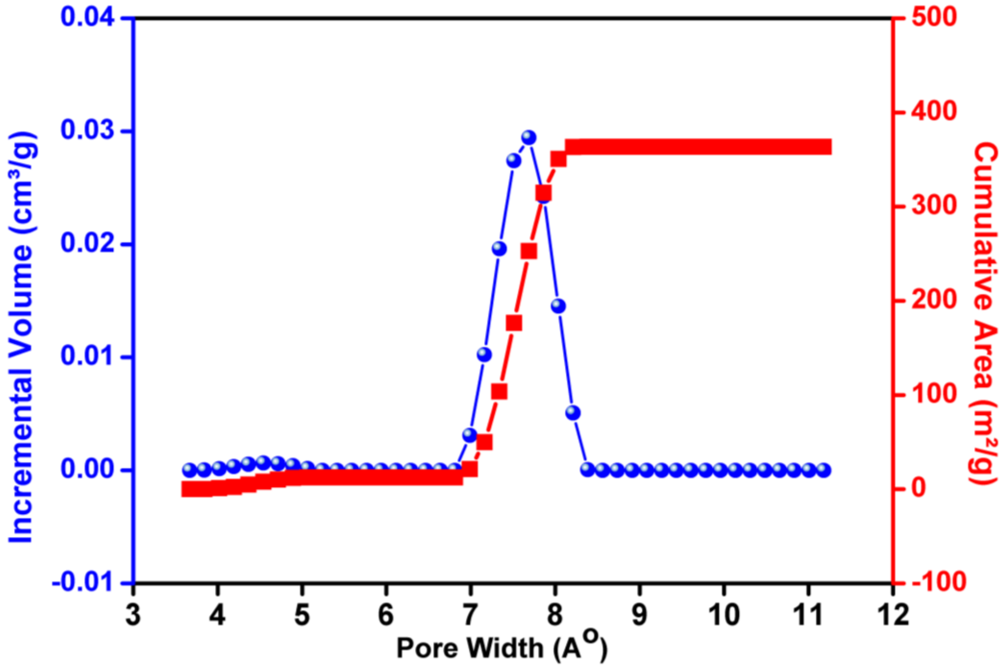

Figure S28. Pore size distribution (NLDFT Slit pore model) of **2** calculated using the 273 K CO_2 adsorption isotherm.

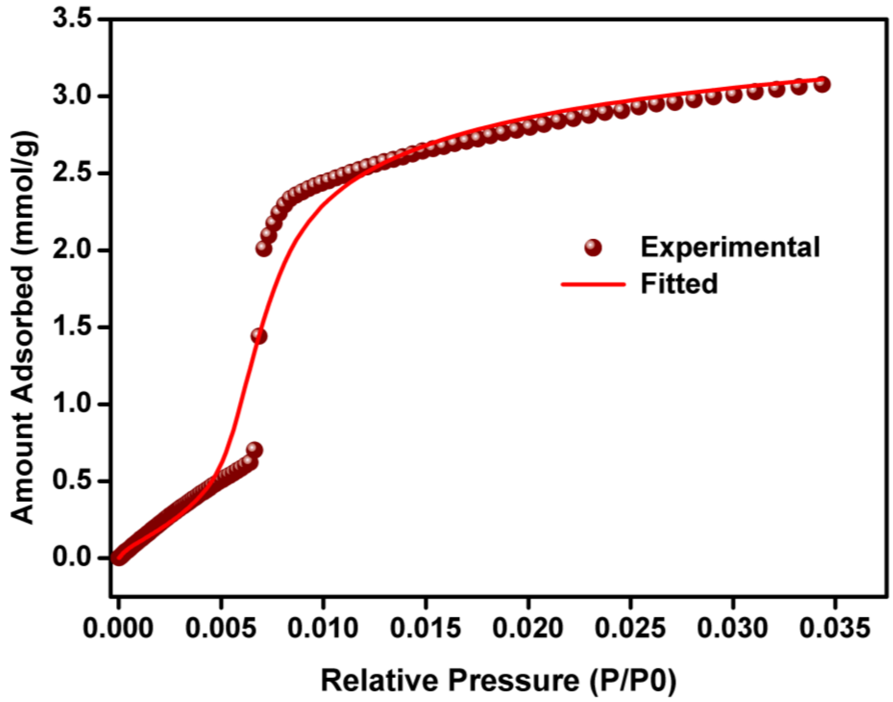

Figure S29. NLDFT fitting comparision for **2**. Note that an average fit was obtained using the whole range of data points of the 273 K CO_2adsorption isotherm.

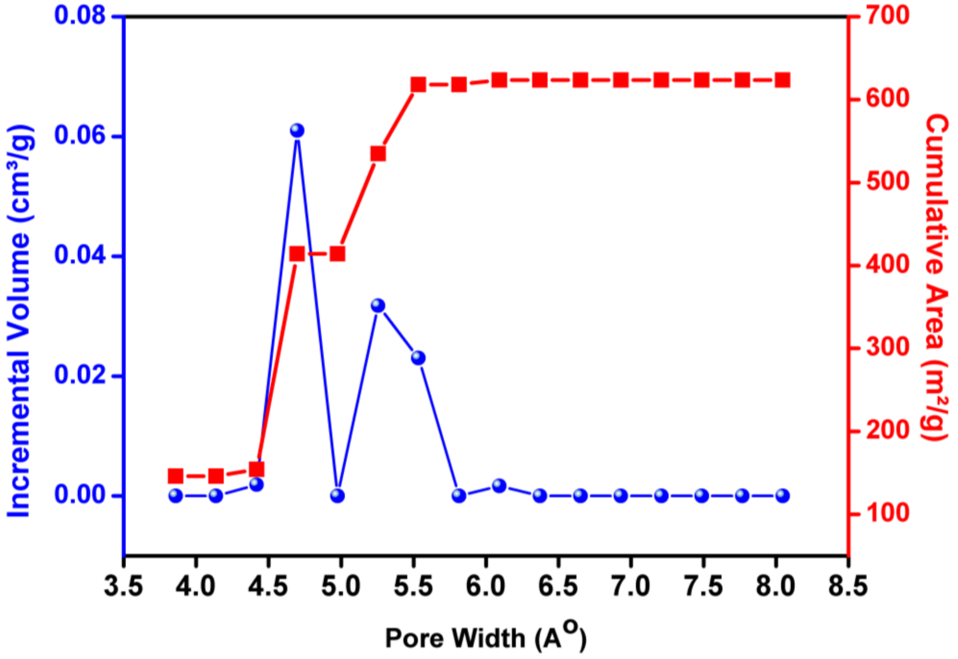

Figure S30. Pore size distribution (NLDFT Slit pore model) of**3** calculated using the 273 K CO_2 adsorption isotherm.

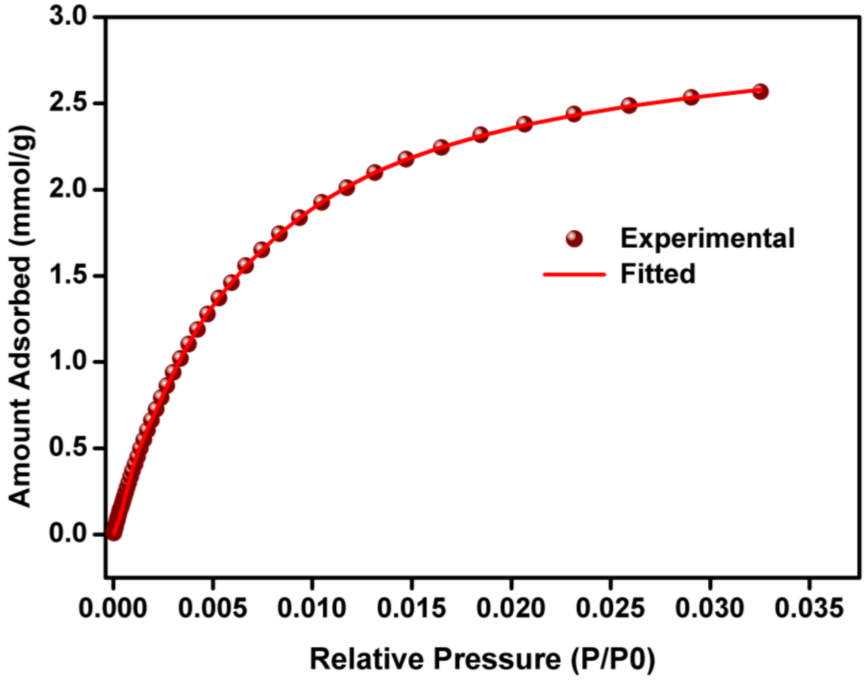

Figure S31. NLDFT fitting comparision for **3**. Note that an average fit was obtained using the entire range of data points of the 273 K CO_2 adsorption isotherm.

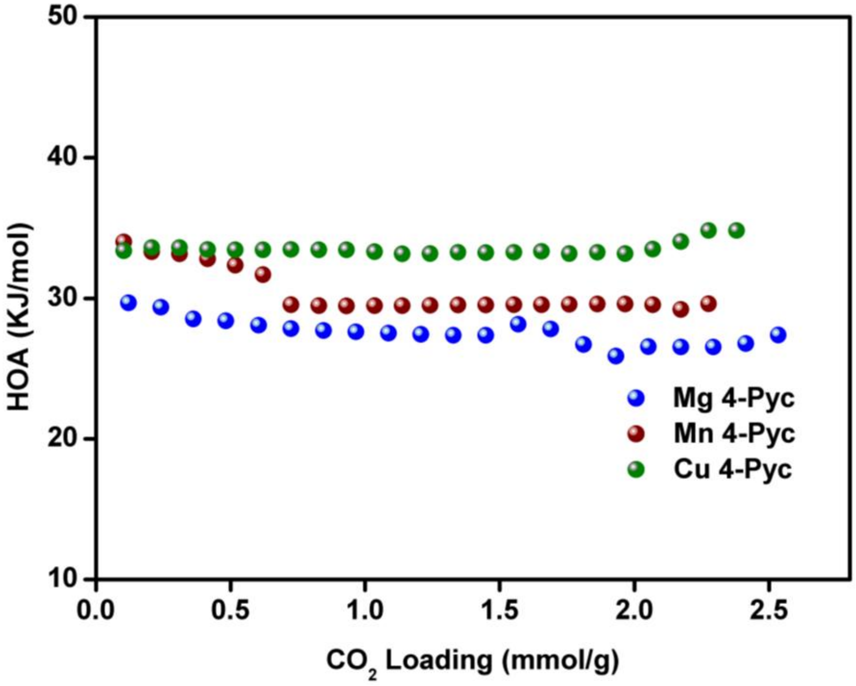

Figure S32. Comparison of the HOA plots obtained from the DFT modeling carried out using the CO_2 isotherms collected at -10°, 0°, +10° and +25° C.

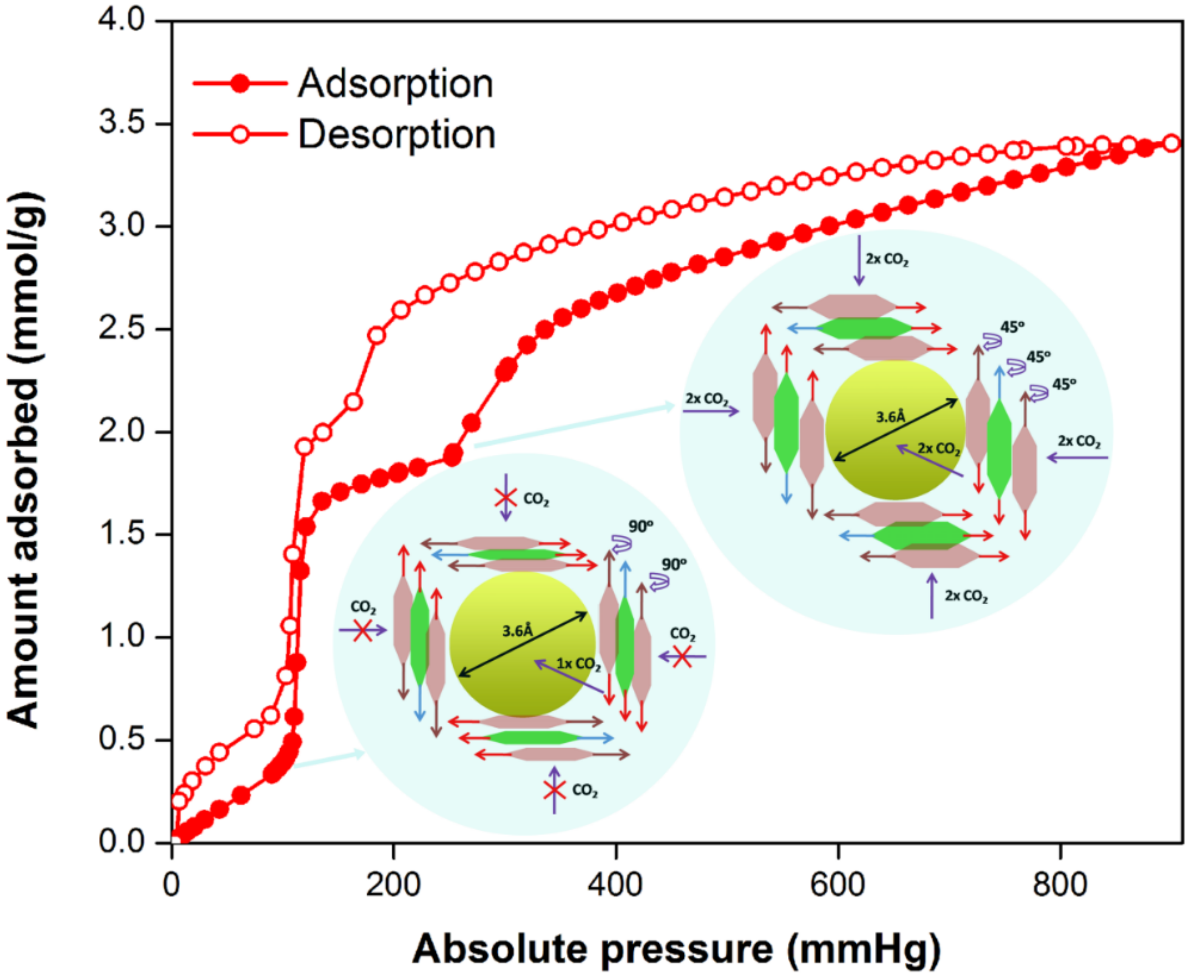

Figure S33. Schematic illustration of the structural rearrangements proposed for the increased accessibility of the ultra-micropores for CO_2 as the pressure is increased. The opening of gate-I (0.1 bar CO_2@273 K) involves the rotation of the relatively weaker Mg-N bonds (2.22 Å) by 90° generating a 1-D access to the ultra-micropore, while the opening of the gate-II (0.3bar CO_2) requires the rotation of both the weaker and relatively stronger Mg-N bonds (2.22 and 2.20 Å) by about 45° to achieve optimal orientation favoring the three-dimensional access to the micropore. Note that the pore dimension does not change during the entire process and the CO_2 capacity of the material jumps up significantly. Green arrows: Mg-N bond distance: 2.22 Å; Red arrows: 2.20 Å and Blue arrows: Mg-Carboxylate. Purple arrows show accessibility for CO_2 to the ultra-micropore.

5. ***Rate of adsorption studies- self-diffusion coefficients calculations and analysis***

Diffusion coefficient determination from Rate of Adsorption (ROA) measurements: An extremely high resolution rate of adsorption measurement was carried out using the ASAP2020HD instrument at 273 K in the pressure range of 0-1 bar. The diffusion coefficient was calculated as a function of CO_2 partial pressure. For this purpose, 10 different loading points were used and each of the ROA data was fitted to a spherical pore model[¥]:

$$F = 1 - \frac{6}{\pi^2} \sum_{n=1}^{\infty} \frac{1}{n^2} \mathrm{Exp}\,(-n^2 \pi^2 \tau)$$

F = fractional uptake; τ = non-dimensional time given by $\tau = Dt/R^2$, where R= particle size; t= time (secs); D = apparent diffusivity.

The single-component diffusion coefficient was estimated to be $7.45 \times 10^{-8}\ m^2s^{-1}$ taking the average of these eight points. Note: the kinetics of the low loadings (<1 mmol/g) were extremely hard to model.

[¥] Kourosh Malek and Marc-Olivier Coppensa), *J. Chem. Phys.*, Vol. 119, 2801 (*2003*); Adsorption analysis and equilibria and kinetics, D. D. Do, Imperial College Press, Ed. 2008.

6. Computational Details

Grand Canonical Monte Carlo (GCMC) simulations were performed with *FastMC* an in-house developed codeS1based upon the open source DL_POLY 2S2 molecular dynamics package. The number of production steps used was 107 after an initial equilibration stage of 106 steps for each gas pressure point on the isotherm. A cut-off of 12.5 Å was used for long range interactions which were calculated using a Ewald summation. For pressures less than 1 bar, the ideal gas pressure was used in the Monte Carlo guest insertion and deletion criteria. Conversely, pressures greater than 1 bar was corrected for fugacity by evaluating the uptake based on pressures fitted to the Peng-Robinson equation of stateS3. A 2x2x3 supercell was used for the GCMC simulations.GCMC calculations were performed with the framework held fixed while the gas guest molecules were assumed to be rigid. The electrostatic energetic contributions were determined by partial atomic charges assigned to each atom calculated with the REPEAT methodS4using the DFT derived electrostatic potential. Dispersive and steric repulsive interactions were included by a 12-6 Lennard-Jones (L-J) potential for each atom. The ε and σ parameters for the framework were taken from the Universal Force Field (UFF).S5The ε and σ

parameters defining the non-bonded interaction of N2 were taken from NIMFS6 which was developed to fit to experimental N2 adsorption isotherm data in MOFs. In this a three site charge model for N2 (N = -0.482e, COM = +0.964e) that accounts for the quadrupole moment of the molecule.S7. The ε and σ parameters of CO2 were taken from García-Sánchez et al.S8which were developed to fit experimental adsorption isotherm data in zeolite frameworks. The C-O bond length (1.149 Å) and partial charges on CO2 atoms (C = +0.6512e, O = -0.3256e) was used. Lennard-Jones parameters of all atom types are given in table S3. We have found this combination of force field potentials generally provides good agreement with experimental adsorption isotherms, particularly for small pore MOFs.[S9-11]

Table S3. Lennard-Jones parameters for framework atoms from the UFF forcefield, CO_2 guest molecules, and N_2 guest molecules.

Forcefield	Atom	ε / kcal mol^{-1}	σ / Å
UFF	C	0.1050	3.4309
UFF	O	0.0600	3.1181
UFF	N	0.0690	3.2607
UFF	Mg	0.0150	2.5248
García-Sánchez *et al.*	O (CO_2)	0.1702	3.0170
García-Sánchez *et al.*	C (CO_2)	0.0595	2.7450
NIMF	N (N_2)	0.0784	2.4549

The initial experimental crystal structure of 1 had disorder with respect to the orientation and direction of the organic SBU. The SBU could either bind the metal center via the nitrogen of the pyridine ring or the oxygen of the carboxylic acid, which resulted in the observed disorder. Of all possible combinations of the organic SBU orientations, only 3 had no serious steric overlap. These three structures had almost identical isotherms with the greatest difference in uptake being only 0.1 mmol/g through the pressure range from 0-1 bar. The structure with the least symmetry was used.

Periodic density functional theory (DFT) was performed with the VASP package[S12-S14] using the PBE exchange-correlation functional[S15]. PAW pseudopotentials[S16] were used in a plane wave basis set with a kinetic energy cut-off of 520 eV. All calculations were spin polarized and dispersion corrected with the reciprocal space sampled with a single Γ-centered k-point. Empirical dispersion corrections of Grimme[S17] were included in both energy and force calculations with the default scaling factor of 0.75, as parameterized by Grimme, for the PBE functional.

Molecular dynamics simulations were performed with the GROMACS package[S18]using the same force field as for the GCMC simulations for the guest molecules. For the framework, our modified force field is described below.

Searching the Conformational Space

From the crystal structure, it is apparent that a stable structure shows the linkers can exist in a perpendicular orientation to each other. The first step was to take a look at the two “extreme” orientations where the linkers are either “face-face” orientation which would cause the pore to shrink, or where the linkers are in a “side-side” orientation which would cause the pore to open up. The uptake as a function of linker rotation simulated at 1 bar, and 298 K was calculated was shown in Figure S34A.

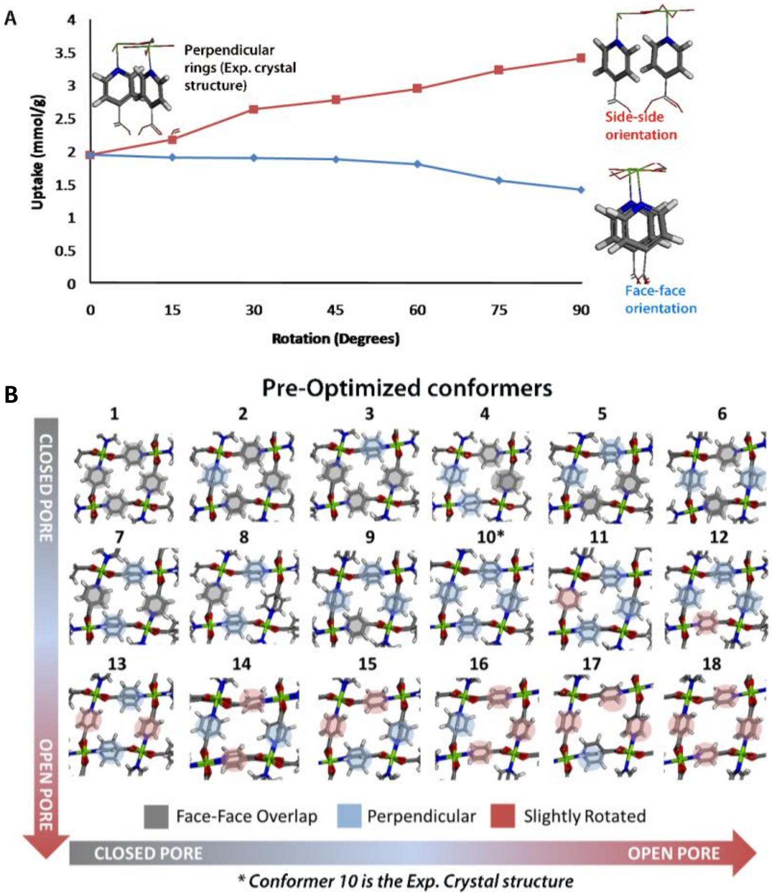

Figure S34. A) Simulated uptake of **1** as a function of rotation of linker for rotation to side-side and face-face orientations. B**)** The 18 conformations for which DFT optimizations were initiated from. The structures are color coded to show the orientation of the linkers whereby grey is face-face overlap as shown in the closed pore structure, blue is perpendicular overlap as shown in the crystal structure, and red is slightly rotated orientation was shown in the open pore structure.

The simulated isotherm was calculated for both “extreme” orientations where the side-side linker orientation is the open pore structure and the face-face orientation is the closed pore structure. The closed pore structure had no uptake, while the open pore structure with an uptake ofabout 5 mmol/g at 1 bar and 273 K. We note that the geometry of these two structures was not optimized and that particularly for the open pore structure there were significant steric interactions.

Following an examination of the two extremes, we performed an exhaustive search of the possible conformations of the pyridyl rings in the pores of **1**. 18 different starting conformations were examined as shown in Figure S34B, each with different combinations of the rings rotated from closed to open positions. It was found that regardless of starting orientation all conformers optimized to five main structures as discussed in the main text (Figure 3A, main text).

Fitting the Torsional Potential of the Pyridyl Rings in 1

In this work, we wanted to examine the dynamics of the pyridyl rings in the MOF 1. However, a reliable classical potential does not exist for this structure, we so modified the UFF force field such that the potential surface of the pyridyl ring matched that from a DFT calculation. First step was to obtain a reference potential at the DFT level. A truncated model system, shown in Figure S35A was used for this purpose where one pyridyl ring was 'isolated' from the MOF and the dangling bonds were capped with hydrogen. A DFT torsional scan of the full rotation of the pyridyl ring in the truncated model system was performed. We retained the default UFF O-C-C-C torsion and modified the O-Ni-N-C torsional potential such that the overall potential best matched that of the DFT calculation. Thus, the target potential is given by:

$$E_{target} = E_{DFT} + (E_{UFF} - E_{OCCC}) \qquad \text{S1}$$

where E_{DFT} is the relative energy resulting from the DFT torsional scan of the model system, E_{UFF} is the energy as calculated by the default forcefield of the torsional scan and E_{OCCC} is the default UFF torsional potential of the O-C-C-C torsion in the model system. For the MD simulations, we used the GROMACS package[15], which uses a cosine functional form for the dihedral torsional potential of the form $V_{d(\phi ijkl)} = k\phi(1 + \cos(n\phi - \phi_s))$ where k is the dihedral constant in kJ/mol, n is the multiplicity, ϕ is the equilibrium dihedral angle in degrees. The modified potential was fitted to the target potential by a least squares fit giving the following constants: $k = 2.1281$ kJ/mol and $\phi = 164.0899^o$. The PES as calculated by DFT and by the fitted UFF potential is shown in Figure S35B and shows a reasonable fit in terms of the rotational barrier being ~10 kcal/mol.

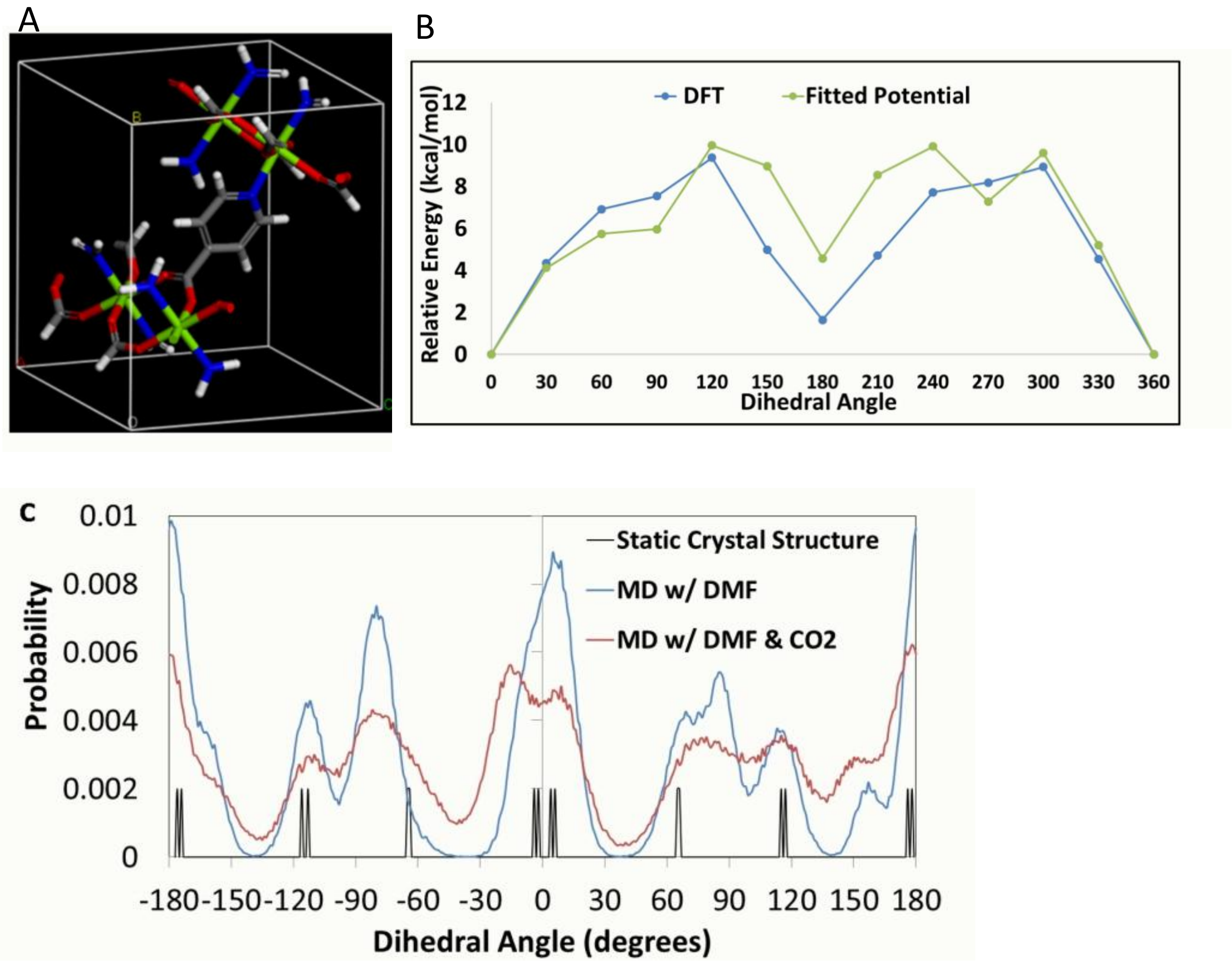

Figure S35. A) The truncated model system of **1** used to calculate the potential energy surface of pyridyl ring rotation and B) Plot of the dihedral scan of the pyridyl ring in the truncated model calculated at the DFT level and with our fitted UFF potential. C) Dihedral angle distributions from 1 ns MD simulations of **1** saturated with DMF (blue) and with a DMF/CO_2 mixture (red).

Validation of the Modified Potential

In order to examine the accuracy of the modified potential, a few tests were done. The first test was to see whether or not the modified potential recreated the crystal structure under similar conditions. Thus, a 1 ns MD simulation with 1 fs time step was performed with the crystal structure with DMF in the pores as the starting initial configuration in a 3 x 2 x 2 supercell. A temperature was 100K was utilized recreate experimental conditions. The forcefield parameters for DMF were taken from the work of Vasudevan et al.[S19] During this MD simulation, the crystal structure is retained throughout. More quantitatively, we examined the distribution of pyridyl dihedral angles and compared it to those values in the experimental crystal structure as given in Figure S35C. The peaks in the dihedral distribution from the MD simulation are in reasonable agreement with that from the static crystal structure. We also performed a similar MD simulation with 2/3 of the DMF replaced by CO_2. The dihedral distribution is similar to that of the full DMF distribution, except that the peaks are much broader showing a loss of order.

Finally, the energetics of the MD structures obtained from the modified forcefield was compared. A 1ns MD simulation at 100k was performed on a 3 x 1 x 1 supercell using the modified forcefield with the crystal structure as the initial configuration. The initial crystal structure and final MD structure were optimized using the modified forcefield in GROMACS. The force field gave an energy difference between the two structures to be 15.09 kcal/mol. These same two structures were then geometry optimized at the DFT level giving an energy difference of 17.5 kcal/mol, in reasonable agreement with the force field.

Binding Sites and Energetics

The binding sites were calculated for the optimized crystal structure, **1c**, and the partially open structure, **1d**, from the conformational search described in the main text. It was hypothesized that the crystal structure conformation, **1c**, corresponds to the structure after the first gate opening between ~0.2-0.4 bar at 273 K and that the CO_2 binding should afford enough energy to alter the conformation of the pyridyl rings to induce the gating to the partial open structure **1d**. The energy difference between **1c** and **1d** calculated at the DFT level was only 2.3 kcal/mol, so one would expect the energy of CO_2 binding to be able to overcome this. Nonetheless, to substantiate the hypothesis, we examine the CO_2 binding sites, and the binding energies associated with conformers **1c** and **1d**.

At 0.325 bar, the CO_2 binding sites of the crystal structure conformation, **1c**, were determined by fitting the maxima of the probability distributions from the GCMC simulations. The CO_2 molecules were placed in the maxima and then optimized with the same force field that the GCMC simulations were performed with. Using this procedure two strong binding sites per unit cell were identified, which corresponds to the loading at this pressure. Figure S36A shows the binding sites which are equivalent. The binding energy of each of these sites were found to be 11.05 kcal/mol. For structure 1d, three binding sites were identified as shown in Figure S36B at 1 bar and 273 K. It is important to note that these binding sites are not mutually exclusive, so that all can be occupied at once. The individual binding energies are only slightly smaller than that observed with conformation **1c**.Thus, the addition of the third CO_2 molecule can easily overcome the energy difference between conformation **1c** and **1d** and the entropic cost of bringing the molecule out of the gas phase.

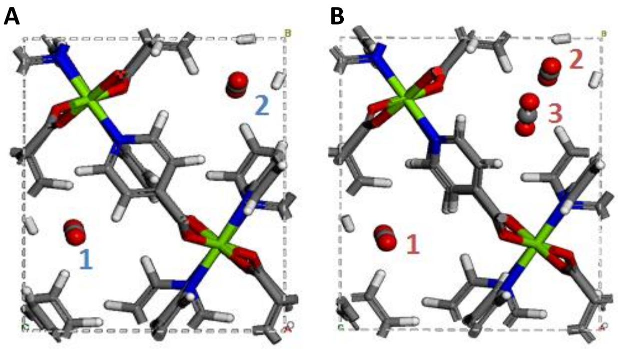

1=**2** 11.1 kcal/mol

1 10.9 kcal/mol
2 10.1 kcal/mol
3 11.0 kcal/mol

Figure S36. A) Binding sites identified for the crystal structure conformation **1c**. B) Binding sites identified for structure **1d**. Binding energies of the sites are given below the structure.

References for computational section

S1. Boyd, Peter G. (2015) “Computational Highthroughput Screening of Metal Organic Frameworks for Carbon Dioxide Capture and Storage Applications” (Ph.D. thesis, University of Ottawa, Canada) DOI: 10.20381/ruor-4264

S2. Smith, W.; Forester, T. R. “DL_POLY_2.0: A General-Purpose Parallel Molecular Dynamics Simulation Package”*J. Mol. Graph.***1996**, *14* (3), 136–141.

S3. Stryjek, R. & Vera, J. H. “PRSV: An improved Peng-Robinson equation of state for pure compounds and mixtures.”*Can. J. Chem. Eng.***64,** 323–333 (1986).

S4. Campañá, C., Mussard, B. & Woo, T. K. “Electrostatic Potential Derived Atomic Charges for Periodic Systems Using a Modified Error Functional”: *J. Chem. Theory Comput.***5,** 2866–2878 (2009)

S5. Rappe, A. K., Casewit, C. J., Colwell, K. S., Goddard, W. A. & Skiff, W. M. “UFF, a full periodic table force field for molecular mechanics and molecular dynamics simulations” *J. Am. Chem. Soc.***114,** 10024–10035 (1992).

S6. Provost, Bianca (2015) “An Improved N_2 Model for Predicting Gas Adsorption in MOFs and using Molecular Simulation to aid in the Interpretation of SSNMR Spectra of MOFs” (M.Sc. thesis, University of Ottawa, Canada) DOI: 10.20381/ruor-2693.

S7. Potoff, J. J. & Siepmann, J. I. “Vapor–liquid equilibria of mixtures containing alkanes, carbon dioxide, and nitrogen” *AIChE J.***47,** 1676–1682 (2001).

S8. García-Sánchez, A. *et al.* “Transferable Force Field for Carbon Dioxide Adsorption in Zeolites” *J. Phys. Chem. C***113,** 8814–8820 (2009).

S9. Vaidhyanathan, R.; Iremonger, S.S.; Shimizu, G.K.H.; Boyd, P.; Alavi, S.; Woo, T.K. ”Direct observation and quantification of CO2 binding within an amine-functionalized nanoporous solid” Science, 330, 650-653 (2010).

S10. Iremonger, S.S; Liang, J.; Vaidhyanathan, R.; Martens, I.; Shimizu, G.K.H.; Daff, T.; Zein Aghaji, M.; Yeganegi, S.; Woo, T.K. “Phosphonate monoesters as carboxylate-like linkers for metal organic frameworks” J. Am. Chem. Soc., 133, 20048-20051 (2011).

S11. Nandi, S.; De Luna, P.; Daff, T.D.; Rother, J.; Liu, M.; Buchana, W.; Hawrari, A.I.; Woo, T.K.*; Vaidhyanathan, R.* “A single-ligan ultra-microporous MOF for precombustion CO2 capture and hydrogen purification” Science Advances, 11, e1500421 (2015).

S12. Kresse, G. & Hafner, J. “Ab initio molecular dynamics for liquid metals”*Phys. Rev. B***47,** 558–561 (1993).

S13. Kresse, G. “Efficient iterative schemes for ab initio total-energy calculations using a plane-wave basis set” *Phys. Rev. B***54,** 11169–11186 (1996).

S14. Kresse, G. & Hafner, J. “Ab initio molecular-dynamics simulation of the liquid-metal–amorphous-semiconductor transition in germanium” *Phys. Rev. B***49,** 14251–14269 (1994).

S15. Perdew, J. P., Burke, K. & Ernzerhof, M. “Generalized Gradient Approximation Made Simple”*Phys. Rev. Lett.***77,** 3865–3868 (1996).

S16. Blöchl, P. E. Projector augmented-wave method. *Phys. Rev. B***50,** 17953–17979 (1994).

S17. Grimme, S. Semiempirical GGA-type density functional constructed with a long-range dispersion correction. *J. Comput. Chem.***27,** 1787–99 (2006).

S18. Abraham, et al. “GROMACS: High performance molecular simulations through multi-level parallelism from laptops to supercomputers” *SoftwareX*, 1-2,19-25(2015).

S19. Vasudevan, V.; Mushrif, S. H. “Force field parameters for N,N-Dimethylformamide (DMF) revisited: Improved prediction of bulk properties and complete miscibility in water” *J. Mol. Liq.* **206**, 338-342 (2015)